



A new visible light active multifunctional ternary composite based on $\text{TiO}_2\text{--In}_2\text{O}_3$ nanocrystals heterojunction decorated porous graphitic carbon nitride for photocatalytic treatment of hazardous pollutant and H_2 evolution

Zhifeng Jiang, Deli Jiang, Zaoxue Yan, Dong Liu, Kun Qian, Jimin Xie*

School of Chemistry and Chemical Engineering, Jiangsu University, Zhenjiang 212013, PR China

ARTICLE INFO

Article history:

Received 21 November 2014
Received in revised form 27 January 2015
Accepted 31 January 2015
Available online 2 February 2015

Keywords:

$\text{TiO}_2\text{--In}_2\text{O}_3$
Graphitic carbon nitride
Photocatalysis
Water treatment
 H_2 -production

ABSTRACT

Novel $\text{TiO}_2\text{--In}_2\text{O}_3\text{@g-C}_3\text{N}_4$ hybrid system was synthesized by a facile solvothermal method. The photocatalytic activity of the $\text{TiO}_2\text{--In}_2\text{O}_3\text{@g-C}_3\text{N}_4$ hybrid material was evaluated via degradation of RhB and hydrogen-production. It could be found that $\text{TiO}_2\text{--In}_2\text{O}_3\text{@g-C}_3\text{N}_4$ ternary composites exhibit the highest RhB degradation rate, which was 6.6 times than that of pure $\text{g-C}_3\text{N}_4$. As expected, the H_2 -generation rate of the as-prepared ternary materials was found to increase by 48 times than that of pure $\text{g-C}_3\text{N}_4$. The enhanced activities were mainly attributed to the interfacial transfer of photogenerated electrons and holes among TiO_2 , In_2O_3 and $\text{g-C}_3\text{N}_4$, leading to the effective charge separation on these semiconductors, which were evidenced by photoluminescence spectroscopy, electrochemical impedance spectroscopy and photocurrent analysis. The photocatalytic mechanism and photostability of the ternary hybrid materials were also proposed. This work may provide a stepping stone towards the design and practical application of multifunctional hybrids photocatalysts in the photocatalytic degradation of pollutions and hydrogen generation.

© 2015 Elsevier B.V. All rights reserved.

1. Introduction

Environmental pollution and the energy crisis have become two pivotal issues for human society and seriously threatens the existence of terrestrial lives [1,2]. Heterogeneous photocatalysis has been recognized as a potential strategy for the production of environmental remediation and clean energy due to the economical usage of catalysts and solar energy [3–8]. Particularly, anatase TiO_2 , one of the most important wide-band-gap semiconductors, has attracted considerable attention in the field of catalysis, sensing, hydrogen generation, optics and optoelectronics due to its abundance, chemical stability, environmental friendliness and low cost [9–13]. However, the band gap energy of anatase TiO_2 (3.0–3.2 eV) requires UV light to be excited, and thus only a small portion of solar light is absorbed in the UV region [14–18]. Moreover, the rapid recombination of electron–hole (e^- – h^+) pairs after excitation may lead to the low overall efficiency [19–22]. The construction of heterojunctions by coupling TiO_2 with another narrower bandgap

semiconductor with matched energetic levels of valence band (VB) and conduction band (CB) can not only extend the visible light response of TiO_2 -based catalysts but also favor the e^- – h^+ separation, consequently improving the quantum efficiency [23–33].

Indium oxide (In_2O_3) is known as an important *n*-type semiconductor with an indirect bandgap of 2.8 eV, and has been proved to be an efficient sensitizer to extend the absorption spectra of oxide semiconductor photocatalysts from UV region into visible light region [34–36]. Since the CB and VB positions of In_2O_3 (~ -0.6 eV and $\sim +2.2$ eV, respectively, vs. NHE) [37,38] are both higher than those of TiO_2 (~ -0.3 eV and $\sim +2.9$ eV, respectively, vs. NHE) [39], the formation of $\text{TiO}_2\text{@In}_2\text{O}_3$ heterojunction allows for the effective interfacial charge transfer. The coupling of TiO_2 with appropriate In_2O_3 contents have been proved to possess enhanced photocatalytic activities as compared with single TiO_2 since In_2O_3 helps increase photochemical responses of TiO_2 by altering band gap energy, expediting electron transfer, and reducing recombination of photogenerated charge carriers [40–43]. However, TiO_2 and In_2O_3 nanoparticles (NPs) are easily aggregated to minimize their surface area due to their high surface energy, resulting in a remarkable reduction in their photocatalytic activities. In order to solve the problem of agglomeration and/or enhanced the photocatalytic

* Corresponding author. Tel.: +86 11 88791708; fax: +86 11 88791800.
E-mail address: xiejm391@sohu.com (J. Xie).

activities, these NPs have been immobilized onto various supports including graphene [44], silica [45], graphitic carbon nitride ($g\text{-C}_3\text{N}_4$) [46]. Among these materials, $g\text{-C}_3\text{N}_4$ [47–53], which is a polymeric semiconductor with visible-light absorption, has recently attracted a great deal of interest in the photocatalytic field. It can not only disperse NPs onto itself but also effectively improve the visible light absorption as well as the separation of charge carriers. The HOMO and LUMO levels of the $g\text{-C}_3\text{N}_4$ are located at -1.2 eV and $+1.5$ eV, which are higher than the CB and VB edges of In_2O_3 , respectively. When the $g\text{-C}_3\text{N}_4$ was further combined with the $\text{TiO}_2/\text{In}_2\text{O}_3$ heterojunction, the excited electrons on the LUMO of $g\text{-C}_3\text{N}_4$ and CB of In_2O_3 can inject into the CB of TiO_2 , and the holes on the VB of In_2O_3 can transfer to the LUMO of $g\text{-C}_3\text{N}_4$, which immensely prolong the lifetime of photoexcited carriers.

Herein, we report a novel $\text{TiO}_2\text{-In}_2\text{O}_3@g\text{-C}_3\text{N}_4$ hybrid system fabricated by a solvothermal method. The photocatalytic degradation of RhB and hydrogen-production as well as the photoelectrochemical properties of as-prepared photocatalysts were extensively investigated and characterized. It could be found that $\text{TiO}_2\text{-In}_2\text{O}_3@g\text{-C}_3\text{N}_4$ ternary composites showed the enhanced photocatalytic activity due to the low recombination rate of photogenerated carriers as well as the high surface area. The possible photocatalytic mechanism and photostability of the ternary hybrid composites were also investigated. This work may provide a stepping stone toward the design and practical application of multifunctional hybrids photocatalysts in the photocatalytic degradation of pollutions and hydrogen generation.

2. Experimental

2.1. Materials

Major chemicals are of analytical grade and obtained from Sinopharm Chemical Reagent Co., Ltd. Indium nitrate ($\text{In}(\text{NO}_3)_3$) were bought from Aladdin Reagent Co., Ltd. All chemicals used in the experiments were used without further purification. Deionized water was used for all experiments.

2.2. Catalyst preparation

2.2.1. Preparation of $g\text{-C}_3\text{N}_4$ powder

The $g\text{-C}_3\text{N}_4$ was synthesized by thermal treatment of 20 g of urea in a crucible with a cover under ambient pressure in air. The precursor was heated to 600°C at a heating rate of $5^\circ\text{C}/\text{min}$ in a tube furnace for 4 h in air. The resulted final light yellow powder was washed with distilled water and absolute ethanol to remove any residual alkaline species adsorbed on the sample surface, and then dried at 60°C for 24 h.

2.2.2. Preparation of $\text{TiO}_2\text{-In}_2\text{O}_3@g\text{-C}_3\text{N}_4$ ternary hybrid materials

$\text{TiO}_2\text{-In}_2\text{O}_3@g\text{-C}_3\text{N}_4$ ternary hybrid materials were prepared as follows. In the first step, 0.5 g of $g\text{-C}_3\text{N}_4$ was added into $\text{C}_2\text{H}_5\text{OH}$ (40 mL) and then placed in an ultrasonic bath for 30 min to completely disperse the $g\text{-C}_3\text{N}_4$. Secondly, 0.5 mmol $\text{In}(\text{NO}_3)_3$, 0.2 mL tetrabutyl titanate (TBT) and 0.1 mL H_2O were added into the above solution and stirred in a fume hood for 10 min. The resultant suspension was sealed in a 100 mL teflon-lined stainless-steel autoclave. The autoclave was kept at 180°C for 12 h in an electric oven. After being cooled to room temperature, the samples were collected by centrifugation, washed with deionized water and absolute ethanol several times, and then dried in a vacuum for 48 h. $\text{TiO}_2@g\text{-C}_3\text{N}_4$ and $\text{In}_2\text{O}_3@g\text{-C}_3\text{N}_4$ were prepared in the absence of $\text{In}(\text{NO}_3)_3$ or TBT, respectively.

2.3. Characterization

The crystal structure and phase purity of the prepared samples were analyzed by X-ray diffraction (XRD) using D8 advance X-ray diffraction (Bruker axs company, Germany) equipped with $\text{Cu-K}\alpha$ radiation ($\lambda = 1.5406 \text{ \AA}$), employing a scanning rate of $0.02^\circ \text{ s}^{-1}$ in the 2θ range from 20 to 80° . Scanning electron microscopy (SEM) and energy-dispersive X-ray spectroscopy (EDS) were performed on a scanning electron microscope (Hitachi S-4800 II, Japan) operated at an acceleration voltage of 10 kV to characterize the morphologies and the compositions of the prepared samples. Furthermore, the morphology and particle size of the products were also examined by transmission electron microscopy (TEM) which was recorded on a JEOL-JEM-2010 (JEOL, Japan) operating at 200 kV. UV-vis diffuse reflection spectroscopy (DRS) was performed on a Shimadzu UV2550 spectrophotometer using BaSO_4 as the reference. The photoluminescence (PL) spectra of the photocatalyst were obtained by a Varian Cary Eclipse spectrometer. The N_2 physical absorption measurements were carried out at 77 K with a NOVA2000e analytical system made by Quantachrome Corporation (USA). The specific surface area was calculated by Brunauer–Emmett–Teller (BET) method. Pore size distribution and pore volume were calculated by Barrett–Joyner–Halenda (BJH) method. X-ray photo-electron spectroscopy (XPS) analysis was measured on an ESCALAB MK X-ray photoelectron spectrometer. The photoluminescence (PL) measurements were carried out using a Hitachi F-4600 fluorescence spectrophotometer.

2.4. Photocatalytic activity for degradation of RhB

The photocatalytic measurement was carried out in an open home-made thermostatic photoreactor. Before light irradiation, a suspension containing 80 mL of 10 mg/L RhB solution and 80 mg of a solid catalyst was sonicated for 10 min and then stirred 1 h in the dark to ensure an adsorption–desorption equilibrium. Then the suspension was irradiated under continuous stirring by using a 350 W Xenon arc lamp and was positioned 20 cm away from the reactor. All the experiments were performed at 25°C under constant stirring. At a given time interval of irradiation, 5 mL of the solution was taken out, and centrifuged for subsequent measurement with a UV-vis spectrophotometer (UV-2450, Shimadzu) at the maximal absorption wavelength of RhB, whose characteristic absorption peaks was 554 nm (λ_{RhB}). To establish the stability of the photocatalysts, the used photocatalyst was recycled for testing subsequent photocatalytic activities as follows. After a photocatalytic experiment, the ternary composite was recovered by washing with distilled water three times, drying at 100°C for 24 h.

2.5. Active species trapping experiments

For detecting the active species during the reaction, tert-butanol ($t\text{-BuOH}$), ammonium oxalate (AO) and 1, 4-benzoquinone (BQ) were used as the hydroxyl radical ($\text{OH}\cdot$) scavenger, hole (h^+) scavenger and superoxide radical ($\text{O}_2^{\cdot-}$) scavenger, respectively. The process was parallel to the former photocatalytic activity experiment with the addition of quencher in the presence of RhB.

2.6. Photoelectrochemical measurements

Electrochemical and photoelectrochemical measurements were performed in three-electrode quartz cells with a 0.1 M Na_2SO_4 electrolyte solution. Platinum wire was used as the counter electrode, and saturated calomel electrodes (SCE) were used as the reference electrodes, respectively. The as-prepared photocatalyst film electrodes on ITO served as the working electrode. Working electrodes were prepared as follows: ITO glass was washed sequentially with

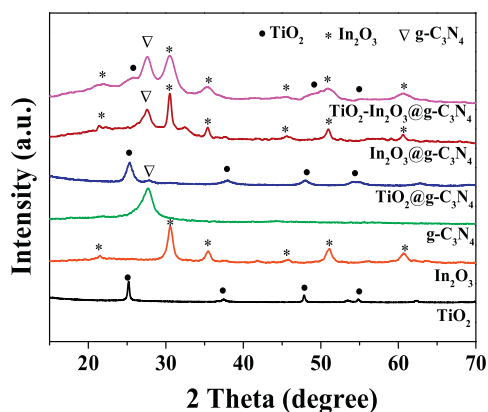


Fig. 1. XRD patterns of as-prepared catalysts.

distilled water, ethanol and acetone in an ultrasonic cleaner for 30 min, 6 μ L, 2.0 mg/mL catalysts aqueous solution was dropped onto the pretreated ITO and dried in air at room temperature to form photocatalysts modified ITO. Electrochemical impedance spectroscopy (EIS) measurements were determined at an AC voltage magnitude of 5 mV with the frequency range of 10^5 – 10^{-1} Hz. A 500 W Xe arc lamp was utilized as the light source in the photoelectrochemical measurements. All electrochemical tests were carried out at room temperature under nitrogen atmosphere.

2.7. Photocatalytic hydrogen evolution

Photocatalytic hydrogen evolution reaction was carried out in a 100 mL three necked Pyrex flask at ambient temperature and atmospheric pressure, and the outlets of the flask were sealed with silicone rubber septums. Four low power UV-LEDs (3 W, 420 nm) (Shenzhen LAMPLIC Science Co., Ltd., China), which were positioned 1 cm away from the reactor in four different directions, were used as light sources to trigger the photocatalytic reaction. The focused intensity and areas on the flask for each UV-LED was ca. 80.0 mW cm⁻² and 1 cm², respectively. The as-prepared sample (50 mg) was dispersed in 80 mL aqueous solution containing 25 vol% methanol for hydrogen evolution. Prior to irradiation, the suspension of the catalyst was dispersed by an ultrasonic bath for 10 min, and then bubbled with nitrogen through the reactor for 1 h to completely remove the dissolved oxygen and ensure the reactor was in an anaerobic condition. The reaction temperature was kept about 293 K. During the whole reaction process, vigorous agitation was performed to ensure the uniform irradiation of the photocatalysts suspension. A 0.4 mL gas was intermittently sampled through the septum, and hydrogen was analyzed by gas chromatography (GC-14C, Shimadzu, Japan, TCD, with nitrogen as a carrier gas and 5 Å molecular sieve column).

3. Results and discussion

3.1. XRD analysis

The XRD patterns of as-prepared binary (TiO₂@g-C₃N₄ and In₂O₃@g-C₃N₄) and ternary (TiO₂-In₂O₃@g-C₃N₄) photocatalysts, as well as the single samples (TiO₂, In₂O₃ and g-C₃N₄) were shown in Fig. 1. The diffraction peaks of TiO₂ were consistent with the values in the standard card (JCPDS, no. 21-1272). The diffraction peaks at 2θ value of 25.3°, 37.8°, 48.1° and 54.9° could be well indexed to (1 0 1), (0 0 4), (2 0 0) and (2 1 1) planes of anatase TiO₂, respectively, indicating that only anatase TiO₂ formed in this case [54]. The XRD pattern of In₂O₃ gave rise to six distinct diffraction peaks at 21.5°, 30.5°, 35.6°, 45.4°, 51.0° and 60.8°, which could be attributed to

the (2 1 1), (2 2 2), (4 0 0), (4 3 1), (4 4 0) and (6 2 2) crystal planes of cubic In₂O₃ (JCPDS, no. 71-2194), respectively [55]. The characteristic peak of g-C₃N₄ around 27.4° could be clearly identified, which was indexed as (0 0 2) diffraction plane. The XRD peak at this degree in g-C₃N₄ was due to the stacking of the conjugated aromatic system [56]. Ternary composite of TiO₂-In₂O₃@g-C₃N₄ exhibit characteristic XRD peaks of TiO₂, In₂O₃ and g-C₃N₄. No impurity phase was observed in the ternary XRD pattern. Thus, it could be confirmed that the ternary hybrid composites present a three-phase composition.

3.2. TEM and SEM analysis

The detailed morphologies and structures about the as-prepared composites were investigated by TEM/HRTEM (Fig. 2) and SEM mapping (Fig. 3) analysis. Fig. 2A shows the pure g-C₃N₄ nanosheets, the smooth and flat layers in the pure g-C₃N₄ sample could be clearly seen, which was consistent with the reported results [56]. Pure TiO₂ and In₂O₃ NPs prepared without g-C₃N₄ are shown in Fig. 2B and C, respectively. The size distributions of TiO₂ (with average size of 62 nm) and In₂O₃ (with average size of 116 nm) were 22–92 nm and 75–146 nm, respectively (Fig. S1A and B). TEM images of TiO₂@g-C₃N₄ and In₂O₃@g-C₃N₄ binary composites were present in Fig. 2D and E. As can be seen from the TEM images, the size distributions of TiO₂ (with average size of 6 nm) and In₂O₃ (with average size of 9 nm) were 4–8 nm and 5–13 nm, respectively (Fig. S1C and D). It can be seen that TiO₂ and In₂O₃ NPs were densely and uniformly distributed on the surface of g-C₃N₄. In addition, the sizes of TiO₂ and In₂O₃ on the surface of g-C₃N₄ were smaller than those of pure TiO₂ and In₂O₃. Fig. 2F showed the typical TEM image of the TiO₂-In₂O₃@g-C₃N₄. It was obvious that the diameters of TiO₂/In₂O₃ NPs were in the range of 10–15 nm and the average diameter of NPs was about 12 nm. Almost on free NPs were found outside of the g-C₃N₄ nanosheets throughout the TEM observation process, indicating the perfect combination between TiO₂/In₂O₃ NPs and g-C₃N₄. The corresponding HRTEM image was illustrated in Fig. 2G. The clear lattice fringes revealed that the single crystalline nature of the NPs on the g-C₃N₄ nanosheet surfaces, and the interplanar spacing matched well the separation of TiO₂ (1 0 1) and In₂O₃ (2 2 2) planes. Fringe lines with 0.35 nm spacing are for the (2 2 2) crystal plane of cubic In₂O₃ and 0.29 nm are corresponding to (1 1 1) facet of anatase TiO₂ [56,57]. Fig. 3 displayed the SEM/EDS mapping images of the as-synthesized TiO₂-In₂O₃@g-C₃N₄. As presented in Fig. 3A, the morphology of the ternary composite was composed of the 3d hierarchical structure, which may possibly obtain a high surface area, thus provide more reactive sites. The formation of the ternary hybrid material was further confirmed by the elemental mapping (Fig. 3B). The maps of C, N, Ti and In were well-defined with sharp contrast. Moreover, the profiles of Ti and In were close to that of C and N, which indicated that the Ti and In elements distribute uniformly and densely throughout the whole composites. Combined with the XRD result, it could confirm that TiO₂ and In₂O₃ were successfully combined with the g-C₃N₄.

3.3. FT-IR analysis

The FT-IR spectra of pure g-C₃N₄ and g-C₃N₄-based composites (Fig. 4) showed all the feature-distinctive stretch modes of aromatic CN heterocycles at 1200–1700 cm⁻¹ together with the breathing mode of the bending vibration of heptazine rings at 808 cm⁻¹, which was consistent with the reported literatures [58–60]. A broad band located in the range from 3600 to 3000 cm⁻¹ corresponded to the stretching modes of terminal NH₂ or NH groups at the defect sites of the aromatic ring [60]. It could be also clearly seen that the main characteristic peaks of g-C₃N₄ appeared

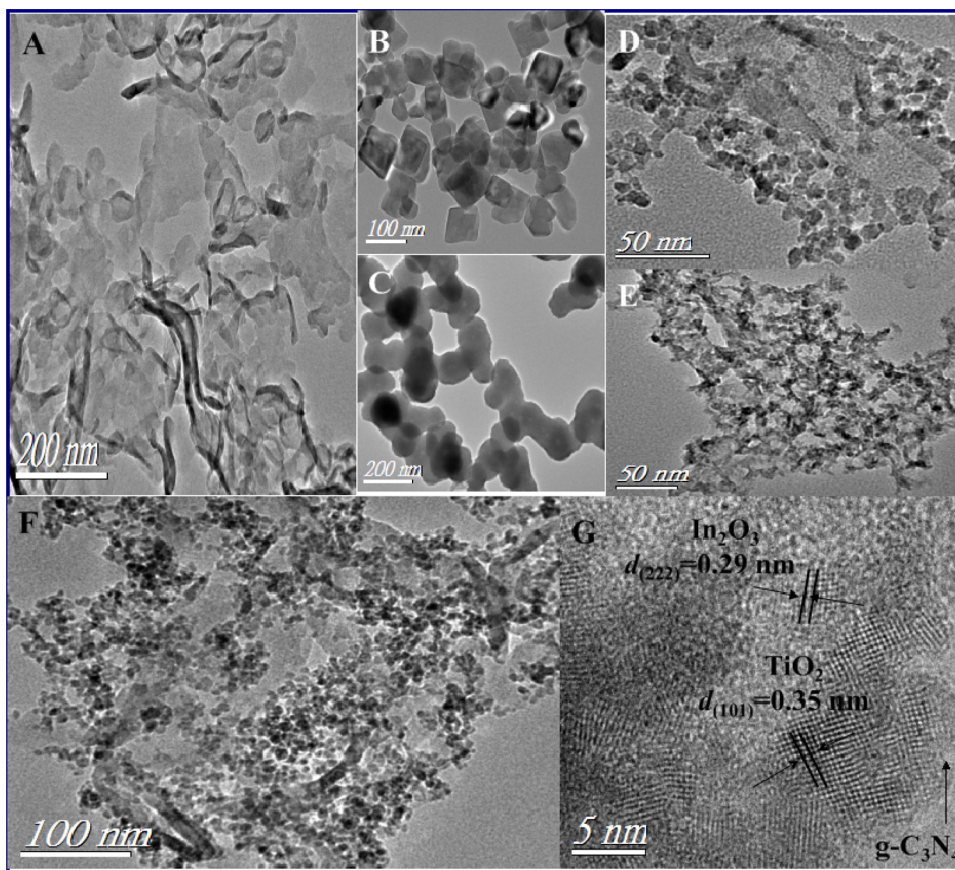


Fig. 2. TEM/HRTEM images of g-C₃N₄ (A), TiO₂ (B), In₂O₃ (C), TiO₂@g-C₃N₄ (D), In₂O₃@g-C₃N₄ (E), and TiO₂-In₂O₃@g-C₃N₄ (F and G).

in TiO₂@gC₃N₄, In₂O₃@g-C₃N₄ and TiO₂-In₂O₃@g-C₃N₄ photocatalysts, which suggested that the structural integrity of g-C₃N₄ remains intact after the deposition of TiO₂ and In₂O₃. The characteristic peaks of g-C₃N₄ did not shift after combination with TiO₂ and In₂O₃ NPs, which has indicated that in the hybrid and ternary composites systems, there were no covalent bonds between g-C₃N₄ and TiO₂-In₂O₃ NPs.

3.4. Raman analysis

Raman spectroscopy was also applied in order to study the structure of TiO₂-In₂O₃ anchoring on the g-C₃N₄ sheets. The Raman spectra of pure g-C₃N₄ and TiO₂-In₂O₃@g-C₃N₄ were shown in Fig. 5. Two peaks for g-C₃N₄ and TiO₂-In₂O₃@g-C₃N₄ located at 1345 cm⁻¹ and 1597 cm⁻¹ were corresponding to D band and G band of graphitic carbon nitride, respectively [61]. The G

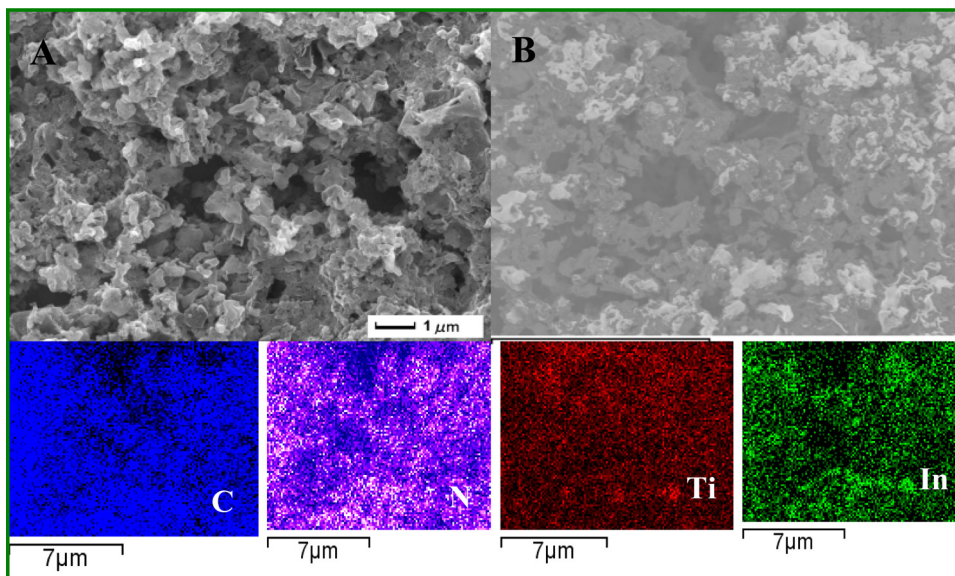


Fig. 3. SEM images and EDS mapping of TiO₂-In₂O₃@g-C₃N₄.

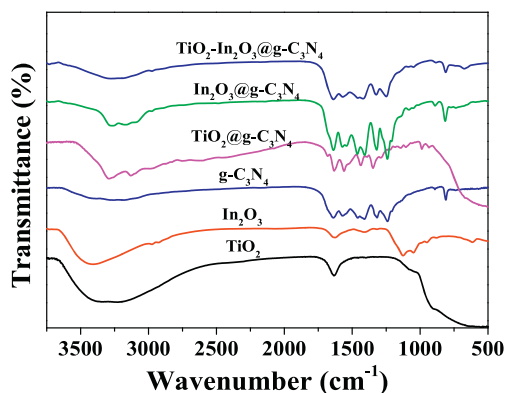


Fig. 4. FT-IR spectra of pure g-C₃N₄ and g-C₃N₄-based composites.

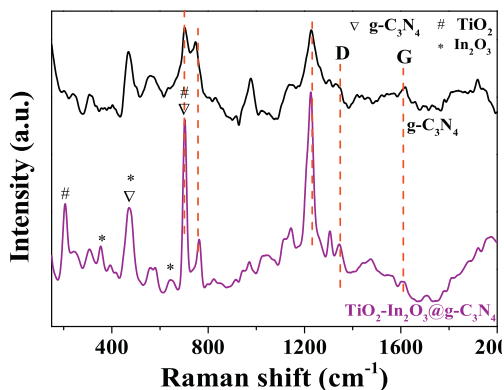


Fig. 5. Raman spectra of pure g-C₃N₄ and TiO₂-In₂O₃@g-C₃N₄.

band, which ascribed to graphite-like sp² microdomains in the as-prepared samples, corresponded to the symmetric E_{2g} vibrational mode of graphite-like structure. In addition, the D band corresponded to disordered sp² microdomains introduced by the linking with N atoms [62,63]. Moreover, comparing with the pure g-C₃N₄, the characteristic peaks for ternary composite at 695, 735 and 1225 cm⁻¹ become stronger, which could be ascribed to the potential enhancing the Raman effect of g-C₃N₄ itself and the charge transfer among TiO₂, In₂O₃ and g-C₃N₄ originating from the coupling effect among TiO₂, In₂O₃ and g-C₃N₄ [63,64]. The peak at 205 cm⁻¹ (E_g), which could be attributed to the characteristic peak of anatase phase, was observed. In addition, three characteristic peaks at 370, 448 and 640 cm⁻¹ were attributed to the vibrational modes of In₂O₃ [65]. All these results further suggested that TiO₂-In₂O₃ NPs were successfully loaded on the surface of g-C₃N₄.

3.5. XPS measurements

XPS was obtained to analyze the surface chemical compositions and chemical states of the resultant crystal of TiO₂-In₂O₃@g-C₃N₄. Fig. 6 provided the high-resolution XPS spectra of C 1s, N 1s, Ti 2p and In 3d for the ternary composite. Fig. 6A shows the C 1s binding energy regions, and two peaks concerning at 288.2 and 284.8 eV are found. The peak centered at 284.8 eV can be ascribed to the C-C coordination of the surface adventitious carbon, whereas the peak at 288.2 eV corresponded to sp³-bonded C in C-N of g-C₃N₄ [66,67]. In the N 1s spectrum (Fig. 6B), several binding energies can be separated. The main signal showed occurrence of C-N-C groups (398.4 eV), tertiary nitrogen N-(C)₃ groups (398.9 eV) and N-H groups (400.5 eV). The peak at 404.5 eV could be related to the charging effects [68,69]. The oxidation state of the Ti element (Fig. 6C) in the products (Ti 2p_{3/2}, binding energy 458.4 eV; Ti 2p_{1/2}, binding energy 464.1 eV) was identical to that of previously

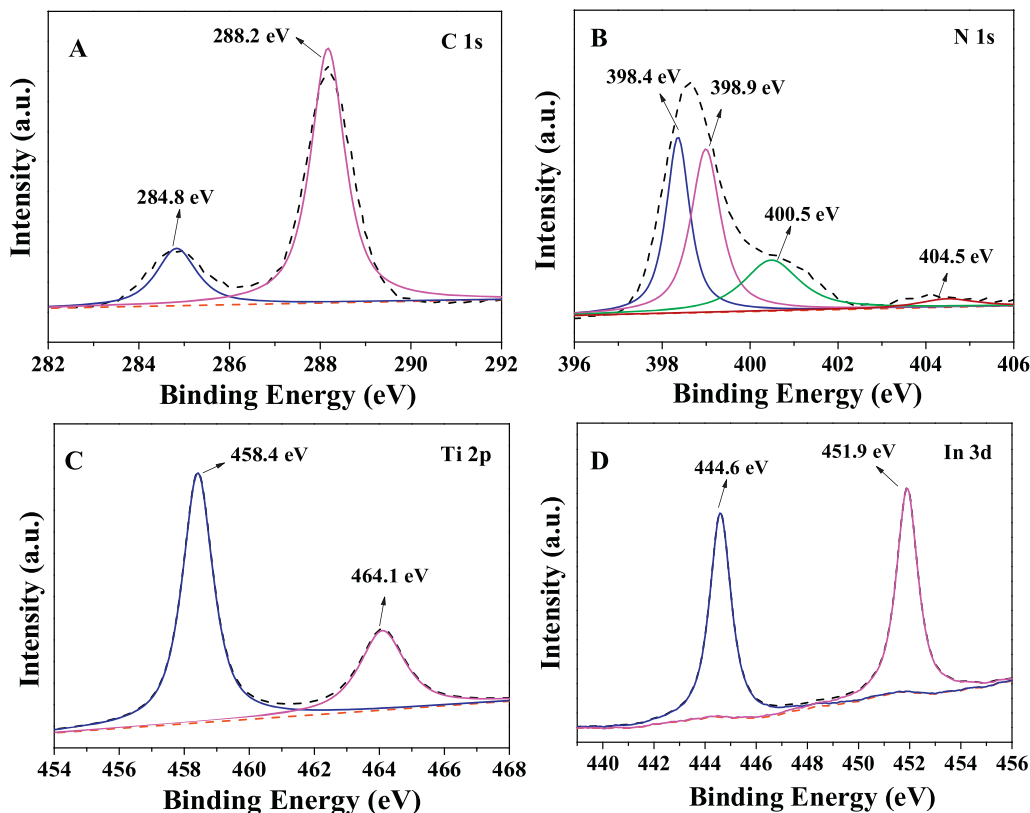


Fig. 6. High-resolution XPS spectra of C 1s, N 1s, Ti 2p and In 3d for the ternary composite.

Table 1

The specific surface areas, pore sizes and pore volumes data of the as-prepared catalysts calculated by BET and BJH methods.

Catalyst	Surface area (m ² /g)	Pore size (nm)	Pore volume (cm ³ /g)
TiO ₂	35.6	1.7	0.114
In ₂ O ₃	38.9	3.8	0.090
g-C ₃ N ₄	49.5	3.8	0.282
TiO ₂ @g-C ₃ N ₄	105.9	9.6	0.395
In ₂ O ₃ @g-C ₃ N ₄	96.4	16.7	0.324
TiO ₂ -In ₂ O ₃ @g-C ₃ N ₄	89.7	3.4	0.335

reported anatase TiO₂ [57]. Moreover, from Fig. 6D, the binding energies of In 3d could be observed at 444.6 and 451.9 eV, which could be attributed to the In³⁺ in In₂O₃. Overall, the three species of TiO₂, In₂O₃ and g-C₃N₄ were successfully obtained in the ternary composite.

3.6. N₂ adsorption–desorption studies

It is well-known that photocatalysts with higher specific surface areas and bigger pore volumes are beneficial for the enhancement of photocatalytic performance because there being more surface active sites for the adsorption of reactant molecules [70]. The N₂ adsorption–desorption isotherms and pore size distribution curves of the as-prepared catalysts were illustrated in Fig. 7. The specific surface areas, pore sizes and pore volumes data of the as-prepared catalysts calculated by BET and BJH methods were summarized in Table 1. All the g-C₃N₄ based photocatalysts are type IV with H3 hysteresis loops according to the IUPAC classification, indicating the presence of mesopores [71–74]. As shown in Table 1, the pure g-C₃N₄ showed a BET surface area of ~49.5 m²/g. Surprisingly, the BET surface area of g-C₃N₄ based composites grew with leaps compared with pristine g-C₃N₄, which might due to the hierarchical structure formed by TiO₂ and In₂O₃ constructed on the surface of g-C₃N₄. The loose spongy structure with a large number of internal spaces leads to a high surface area [60]. The bigger surface area may contribute to a higher photocatalytic activity.

3.7. Optical absorption property

Considering that the visible-light absorption property played an important role in determining the visible photocatalytic activity of semiconductors, the UV–vis diffused reflection spectra studies were performed. Fig. 8 showed the diffuse-reflectance spectroscopy (DRS) of as-prepared TiO₂, In₂O₃, g-C₃N₄, TiO₂@g-C₃N₄, In₂O₃@g-C₃N₄ and TiO₂-In₂O₃@g-C₃N₄. The pure TiO₂ absorbs only ultraviolet light with wavelength shorter than 400 nm. The pure In₂O₃ and g-C₃N₄ samples presented a similar absorption edge at ~450 nm with wide overlap between their absorption spectra. This result was consistent with the previous result that the bandgaps of g-C₃N₄ (2.7 eV) and In₂O₃ (2.8 eV) are narrower than TiO₂ (3.2 eV). The absorption feature of the TiO₂@g-C₃N₄, In₂O₃@g-C₃N₄ and TiO₂-In₂O₃@g-C₃N₄ hybrids showed very little difference with that of pure g-C₃N₄, which also absorbed light with wavelength up to 450 nm.

3.8. Photocatalytic activity towards the degradation of RhB and photostability

RhB is widely used in many industrial fields such as textiles, plastics, paper, coatings and rubber. The discharge of dyes into water has received global concern because of their overall environmental hazards. The removal of RhB from the environment became an important issue [60]. To this end, the photocatalytic activities of as-prepared catalysts towards the decomposition

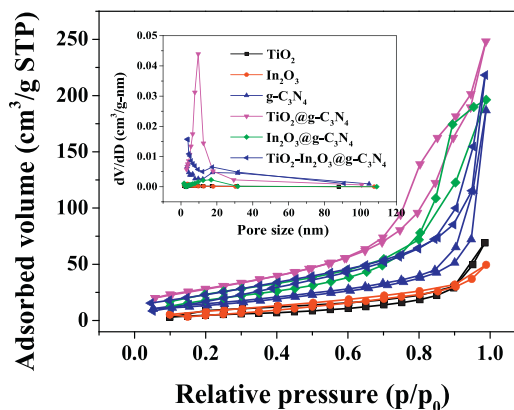


Fig. 7. N₂ adsorption–desorption isotherms and pore size distribution curves of the as-prepared catalysts.

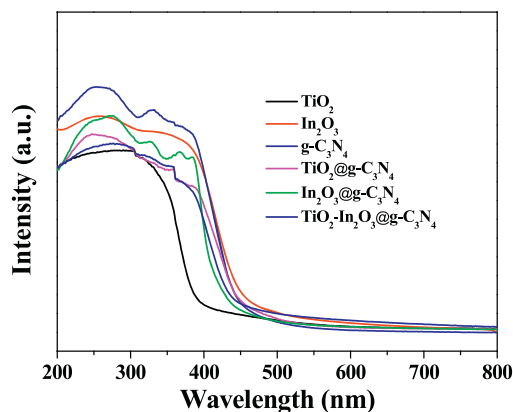


Fig. 8. Diffuse-reflectance spectroscopy (DRS) of as-prepared photocatalysts.

of RhB under visible light were investigated in the present study. According to the adsorption–desorption behavior results of photocatalysts without light irradiation, after 30 min adsorption, there is almost no change in the concentration of dye, which indicates that the adsorption–desorption behavior reached an equilibrium. Fig. 9A showed the variations of the characteristic absorption of RhB ($\lambda = 554$ nm) under visible light irradiation by using TiO₂-In₂O₃@g-C₃N₄ ternary composites as photocatalyst. The characteristic absorption of RhB reduces gradually with prolonging the irradiation time, and the characteristic absorption of RhB is hardly observed after 60 min visible light irradiation. The color of RhB solution changed from red to light red and then disappeared during the reaction. Fig. 9B showed the photocatalytic evaluation of the as-prepared under visible light illumination. As can be seen from Fig. 9B, RhB can only be slightly degraded under visible light irradiation without catalysts, indicating that RhB is a stable molecule and that the photolysis mechanism can be ignored. For a comparison, the plots of RhB dye degradation using TiO₂, In₂O₃ and g-C₃N₄ were included. TiO₂ could degrade less than 40% of the dye after 140 min of visible light irradiation due to this poor visible light absorption capability. In₂O₃ and g-C₃N₄ have shown the similar photocatalytic activity with the degradation efficiency of about 62%. It is interesting that when TiO₂ or In₂O₃ is combined with g-C₃N₄, the photocatalytic activity is increased. The degradation rate using TiO₂@g-C₃N₄ and In₂O₃@g-C₃N₄ were 89% and 72% within 140 min, respectively. The improved photocatalytic activity could be attributed to the formation of the heterojunction as well as the higher surface area. When TiO₂ and In₂O₃ were both deposited on the surface of g-C₃N₄, the photocatalytic activity drastically enhanced (99% within 60 min). This result further indi-

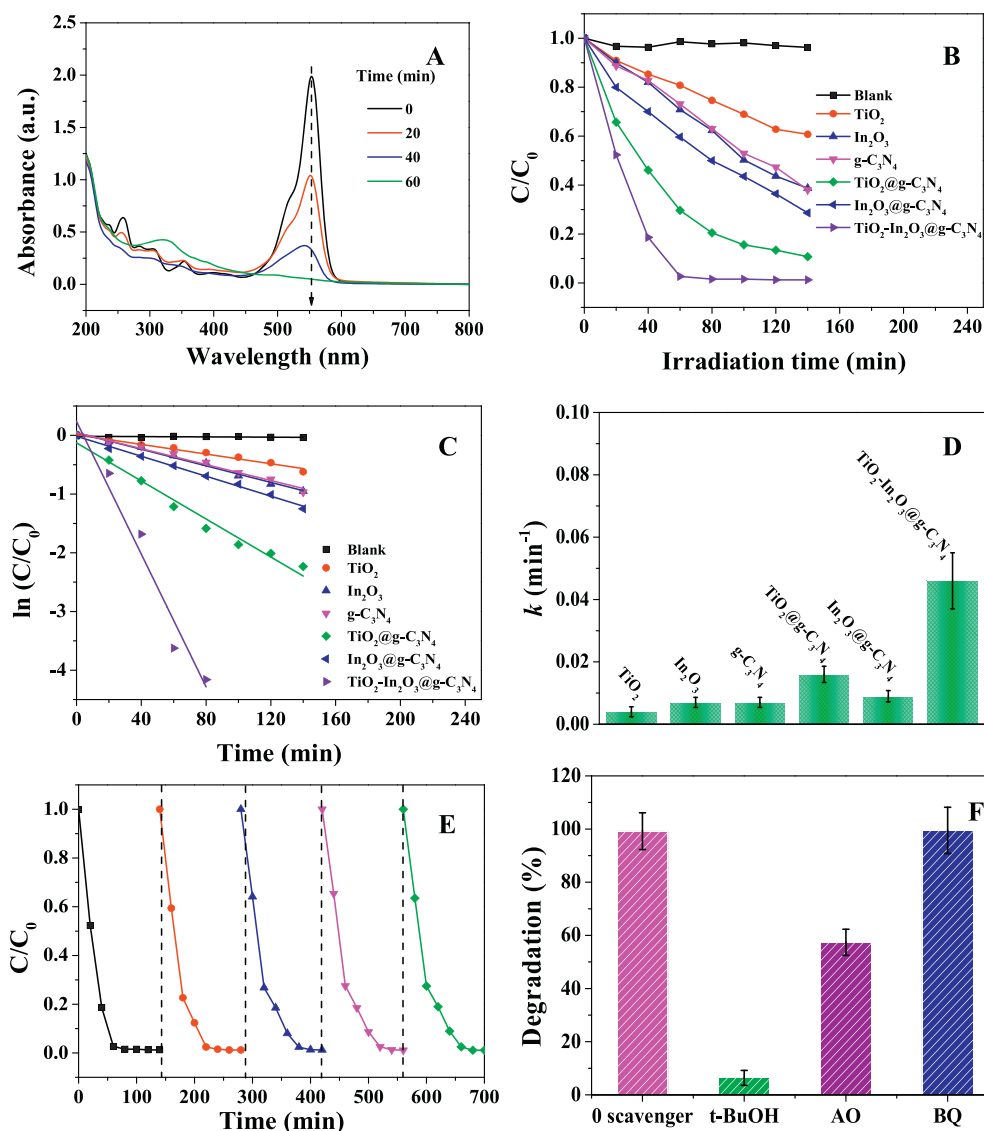


Fig. 9. Photocatalytic activity towards the degradation of RhB (A–D), the possibility of recycling the obtained ternary photocatalyst (E), the influence of various scavengers on the visible-light photocatalytic activity of $\text{TiO}_2\text{-In}_2\text{O}_3/\text{g-C}_3\text{N}_4$ towards the degradation of RhB (F).

cated that the formation of $\text{TiO}_2\text{-In}_2\text{O}_3/\text{g-C}_3\text{N}_4$ ternary structure greatly enhanced the photocatalytic activity since the ternary composite had a similar surface area with the binary composites.

Langmuir–Hinshelwood model has been widely applied for analysis of heterogeneous photocatalytic degradation kinetics of pollutants in the aqueous phase:

$$r_0 = -\frac{dC}{dt} = -\frac{kKC}{1 + KC} \quad (1)$$

where r_0 is the initial reaction rate ($\text{mg L}^{-1} \text{min}^{-1}$), C is the concentration of pollutants (mg L^{-1}), t is the reaction time (min), k is the Langmuir–Hinshelwood reaction rate constant ($\text{mg L}^{-1} \text{min}^{-1}$) and K is the Langmuir adsorption equilibrium constant (L mg^{-1}). At a dilute concentration of pollutants, pseudo-first-order kinetics model could be assumed as shown in Eqs. (2) and (3):

$$r_0 = -\frac{dC}{dt} = -kKC \quad (2)$$

$$\ln\left(\frac{C}{C_0}\right) = -kKt = -k_{\text{app}}t \quad (3)$$

where k_{app} is the apparent rate constant (min^{-1}), and C_0 is the initial concentration of pollutants (mg L^{-1}). The pseudo-first-order rate constants over TiO_2 , In_2O_3 , $\text{g-C}_3\text{N}_4$, $\text{TiO}_2/\text{g-C}_3\text{N}_4$, $\text{In}_2\text{O}_3/\text{g-C}_3\text{N}_4$, and $\text{TiO}_2\text{-In}_2\text{O}_3/\text{g-C}_3\text{N}_4$ are 0.004, 0.007, 0.007, 0.016, 0.009 and 0.046 min^{-1} , respectively. These results indicated that k values for all heterojunction structure are higher than those of pure substances. The photocatalytic decomposition rate of RhB over the $\text{TiO}_2\text{-In}_2\text{O}_3/\text{g-C}_3\text{N}_4$ catalyst was 11.5, 6.6 and 6.6 times the activity over TiO_2 , In_2O_3 and $\text{g-C}_3\text{N}_4$, respectively. More importantly, the photodegradation activity of $\text{TiO}_2\text{-In}_2\text{O}_3/\text{g-C}_3\text{N}_4$ is also higher than many reported $\text{g-C}_3\text{N}_4$ -based photocatalysts. Comparison of the results is shown in Supporting information (Table S1). These results indicated that the formation of $\text{TiO}_2\text{-In}_2\text{O}_3/\text{g-C}_3\text{N}_4$ could greatly enhance the photocatalytic efficiency of $\text{g-C}_3\text{N}_4$.

It is worth pointing out that the stability of the photocatalyst is a crucial but difficult task owing to the leakage of the individual components for the photocatalytic applications in aqueous solution. To confirm the possibility of recycling of the obtained photocatalysts, five recycling experiments were performed with $\text{TiO}_2\text{-In}_2\text{O}_3/\text{g-C}_3\text{N}_4$ ternary composites in the photocatalytic degradation of RhB (Fig. 9E). After each photocatalytic experiment,

the ternary composite was recovered by washing with distilled water three times, drying at 100 °C for 24 h, and then fresh RhB solution was added. As shown in Fig. 9E, no apparent deactivation of the photocatalyst was observed after five consecutive runs. Therefore, the as-prepared $\text{TiO}_2\text{-In}_2\text{O}_3\text{@g-C}_3\text{N}_4$ ternary composites showed an excellent catalytic stability, performing as genuine heterogeneous visible-light-driven photocatalysts for the treatment of organic contaminants in wastewater.

3.9. Free radicals and holes scavenging experiments

In order to understand the photocatalysis mechanism of the heterostructured $\text{TiO}_2\text{-In}_2\text{O}_3\text{@g-C}_3\text{N}_4$ ternary composites, the active species generated during the process of ternary composites-photocatalyzed RhB degradation are identified by free radical and hole trapping experiments. Three different quenchers, *t*-BuOH, AO and BQ were used as the hydroxyl radical (OH^\bullet) scavenger, hole (h^+) scavenger and superoxide radical ($\text{O}_2^{\bullet-}$) scavenger, respectively. Fig. 9F displayed the influence of various scavengers on the visible-light photocatalytic activity of $\text{TiO}_2\text{-In}_2\text{O}_3\text{@g-C}_3\text{N}_4$ towards the degradation of RhB. Compared with scavenger-free system, when 1 mmol of BQ as a scavenger for $\text{O}_2^{\bullet-}$ radical species was added, the degradation rate of RhB was hardly inhibited, indicating the absence of $\text{O}_2^{\bullet-}$ radical species. However, after the addition of 1 mmol *t*-BuOH, the photocatalytic activity for the degradation rate was decelerated drastically (from 99% to 6.4%), indicating the OH^\bullet was the main active species generated in current system. As for the AO-photocatalysis system, the degradation rate was inhibited to some extent, indicating h^+ was another active species that was responsible for the degradation of RhB. Moreover, it is well known that, holes can be adsorbed on the surface of the photocatalyst and can interact with hydroxyl radicals or water molecules to generate OH^\bullet . The above results indicated that OH^\bullet is the most important oxidizing species during the RhB photocatalytic process, and that $\text{O}_2^{\bullet-}$ in the solution is not the main active species.

3.10. Photocatalytic hydrogen evolution activity

Since the as-prepared photocatalysts showed the perfect activity in the degradation of dye, H_2 -production experiment was further carried out to investigate the accurate photocatalytic activity of as-prepared samples. The H_2 evolution experiments were performed by taking 80 mL of a 25 vol% methanol solution and 50 mg of photocatalyst. Before the actual photocatalytic experiment was performed, reference experiments were performed by taking a pure methanol solution in the absence of either photocatalyst or irradiation. H_2 formation was not observed in the control experiment without light irradiation or photocatalyst. This fact indicated that the generation of H_2 results from the photocatalytic activities of as-prepared catalysts, not from other effects. Fig. 10A showed the H_2 evolution plots by TiO_2 , In_2O_3 , $\text{g-C}_3\text{N}_4$, $\text{TiO}_2\text{@g-C}_3\text{N}_4$, $\text{In}_2\text{O}_3\text{@g-C}_3\text{N}_4$ and $\text{TiO}_2\text{-In}_2\text{O}_3\text{@g-C}_3\text{N}_4$ as a function of irradiation time. TiO_2 and In_2O_3 made no contribution to hydrogen evolution under visible light irradiation. As shown in Fig. 10B, the average hydrogen production rates of as-prepared catalysts from the first 4 h of the reaction duration was obtained from Fig. 10A. Pure $\text{g-C}_3\text{N}_4$ obtained from urea also shows negligible visible light H_2 -production activity, although it could absorb visible light. This may probably due to the rapid recombination between electrons and holes, and the fast backward reaction, which was investigated by us.⁶⁰ Remarkably, the hybrid structures of $\text{TiO}_2\text{@g-C}_3\text{N}_4$ (2.0 $\mu\text{mol/h}$) and $\text{In}_2\text{O}_3\text{@g-C}_3\text{N}_4$ (6.2 $\mu\text{mol/h}$) exhibited 11.1 and 34.2 times higher hydrogen generation rate than the pure $\text{g-C}_3\text{N}_4$ (0.18 $\mu\text{mol/h}$).

For the heterostructure formed between TiO_2 (In_2O_3) and $\text{g-C}_3\text{N}_4$ could not only obtain much large surface area than $\text{g-C}_3\text{N}_4$

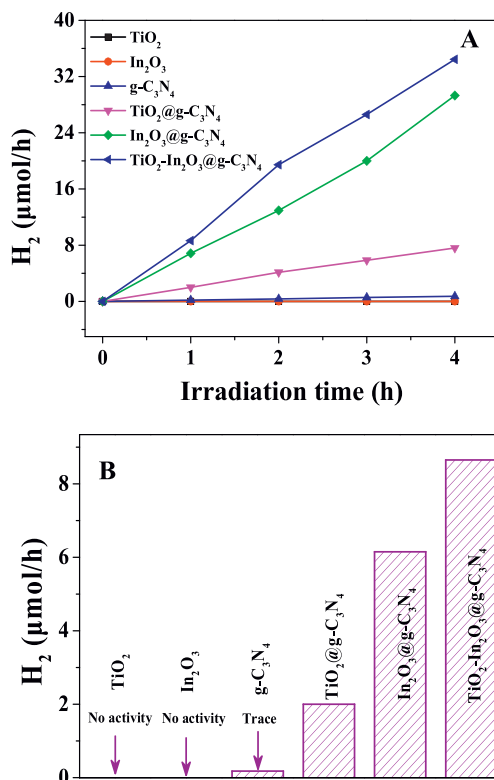


Fig. 10. Photocatalytic hydrogen evolution activity of as-prepared catalysts.

monomer but also minimize the recombination of electron-hole pairs. It was also found that when both TiO_2 and In_2O_3 nanocrystals were decorated on $\text{g-C}_3\text{N}_4$ nanosheets, the transfer of photogenerated electrons would further accelerate (Section 3.11). Owing to these merits, the $\text{TiO}_2\text{-In}_2\text{O}_3\text{@g-C}_3\text{N}_4$ ternary composites did show great photocatalytic activity in hydrogen evolution process. As shown in Fig. 10B, the hydrogen production rate of $\text{TiO}_2\text{-In}_2\text{O}_3\text{@g-C}_3\text{N}_4$ (8.6 $\mu\text{mol/h}$) is 4.3, 1.4 and 48.0 times higher than that of binary hybrids of $\text{TiO}_2\text{@g-C}_3\text{N}_4$ (2.0 $\mu\text{mol/h}$), $\text{In}_2\text{O}_3\text{@g-C}_3\text{N}_4$ (6.2 $\mu\text{mol/h}$) and pure $\text{g-C}_3\text{N}_4$, respectively. In addition, the hydrogen production rate of $\text{TiO}_2\text{-In}_2\text{O}_3\text{@g-C}_3\text{N}_4$ was also higher than many reported $\text{g-C}_3\text{N}_4$ based catalysts, which were summarized in Supporting information (Table S2).

3.11. Photoluminescence spectroscopy

It is widely accepted that the separation efficiency of electrons and holes play a key role in the photocatalytic reaction. PL emission measurement has been widely used to investigate the fate of electron-hole pairs in semiconductor particles because PL emission is known to result from the recombination of excited electrons and holes for some semiconductors. The higher the PL emission intensity indicates the higher the recombination efficiency of the photogenerated carriers and the lower the photocatalytic activity [75–77]. Fig. 11A showed the PL spectra of TiO_2 , In_2O_3 , $\text{g-C}_3\text{N}_4$, $\text{TiO}_2\text{@g-C}_3\text{N}_4$, $\text{In}_2\text{O}_3\text{@g-C}_3\text{N}_4$ and $\text{TiO}_2\text{-In}_2\text{O}_3\text{@g-C}_3\text{N}_4$ photocatalysts excited in 360 nm. The main emission peak was centered at 468 nm for $\text{g-C}_3\text{N}_4$, which could be attributed to the band-band PL phenomenon with the energy of light approximately equal to the band energy of $\text{g-C}_3\text{N}_4$ [77]. After coupling with TiO_2 , In_2O_3 and $\text{TiO}_2\text{-In}_2\text{O}_3$, the position of the emission peak in the PL spectrum was similar to that of $\text{g-C}_3\text{N}_4$, but the emission intensity significantly decreased, which indicated that the binary and ternary composites exhibit slower electron-hole recombination rate compared with pure $\text{g-C}_3\text{N}_4$. In addition, the ternary

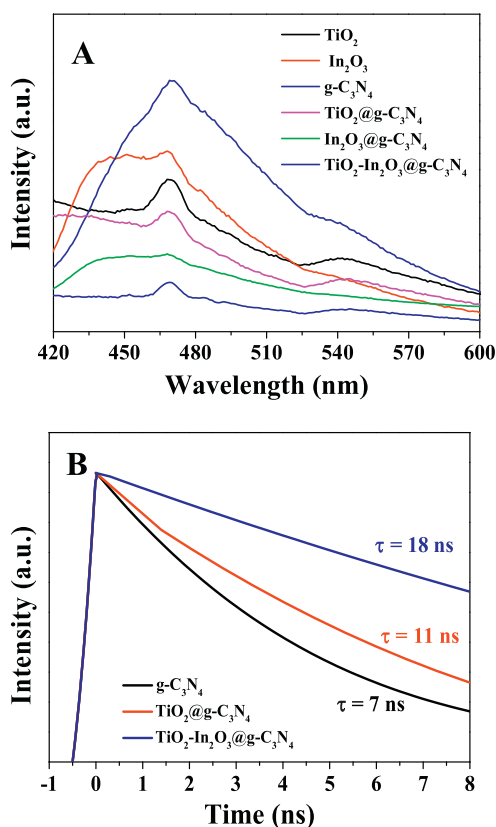


Fig. 11. PL spectra and time-resolved fluorescence decay spectra of as-prepared catalysts.

composites showed the lowest PL intensity among the three as-prepared composites, which indicated the slowest recombination rate of photogenerated charge carriers. These results were consistent with the photocatalytic activity measurements. To better understand the photophysical behavior of the photoexcited charge carriers, time-resolved fluorescence decay spectra of pure $g\text{-C}_3\text{N}_4$, $\text{TiO}_2@g\text{-C}_3\text{N}_4$ and $\text{TiO}_2\text{-In}_2\text{O}_3@g\text{-C}_3\text{N}_4$ were also recorded. Obviously, compared with pure $g\text{-C}_3\text{N}_4$, $\text{TiO}_2@g\text{-C}_3\text{N}_4$ and $\text{TiO}_2\text{-In}_2\text{O}_3@g\text{-C}_3\text{N}_4$ showed slower decay kinetics (Fig. 11B). It was assumed that the increased lifetimes of charge carriers were associated with improved electron transport and/or changes in electronic band structure induced by quantum-confinement effects in the materials [78,79]. A longer PL lifetime means a lower recombination rate of the electron-hole pairs and hence improved photocatalytic activity [79–81].

3.12. Photoelectrochemical measurements

Photoelectrochemical measurements are often used to qualitatively study the excitation and transfer of photogenerated charge carriers in photocatalysis. To understand the photogenerated charge separation and electron transfer performance among TiO_2 , In_2O_3 and $g\text{-C}_3\text{N}_4$, the transient photocurrent responses of all as-prepared material electrodes were recorded for several on-off cycles of light irradiation. The higher photocurrent intensity often leads to better photocatalytic activity. As shown in Fig. 12A, photocurrent over time was detected on visible-light illumination repeated every 20 s at a bias potential of +0.1 V. The photocurrent increased sharply when the light was switched on, and immediately returned to its initial state after the light source was turned off, which was repeatable [75,76]. This result demonstrated that most photogenerated electrons were transferred to the

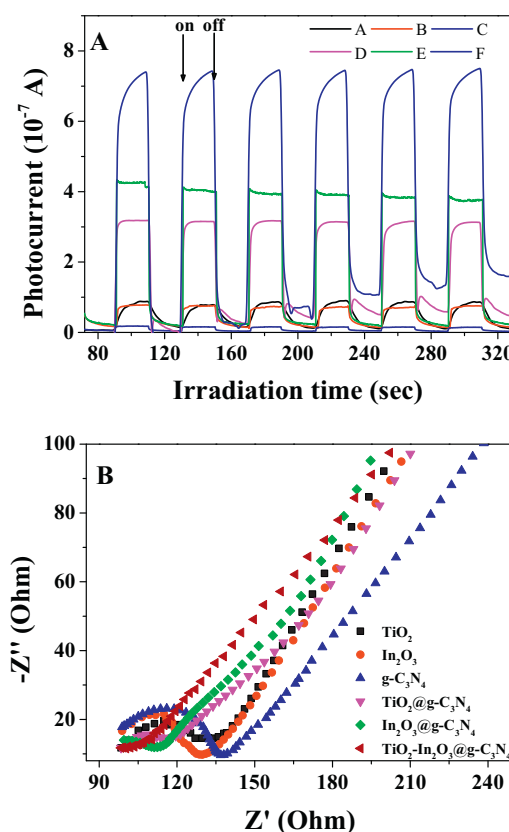


Fig. 12. Time-based photocurrent response (left) and Nyquist plots (right) of $g\text{-C}_3\text{N}_4$ (A), TiO_2 (B), In_2O_3 (C), $\text{TiO}_2@g\text{-C}_3\text{N}_4$ (D), $\text{In}_2\text{O}_3@g\text{-C}_3\text{N}_4$ (E), and $\text{TiO}_2\text{-In}_2\text{O}_3@g\text{-C}_3\text{N}_4$ (F).

back contact across the samples to produce photocurrent under visible light irradiation [77]. The photocurrent of all as-prepared sample/ITO electrodes did not show obvious changes, that is, the photocurrent responses of these electrodes are very stable [81]. As can be obtained from Fig. 12A, $g\text{-C}_3\text{N}_4$ did not show noticeable photocurrent response, and the photogenerated current densities of TiO_2 and In_2O_3 photoelectrodes were very low (less than 10^{-7} A/cm^2). Thus, the mobility of the photogenerated electrons and holes in these materials were low, which enhanced their recombination. On the contrary, $\text{TiO}_2@g\text{-C}_3\text{N}_4$ and $\text{In}_2\text{O}_3@g\text{-C}_3\text{N}_4$ binary hybrid materials showed higher photocurrent densities than those of monomers. This obvious increased photocurrent indicated less recombination and a more efficient separation of photogenerated electron and hole pairs for the $\text{TiO}_2@g\text{-C}_3\text{N}_4$ and $\text{In}_2\text{O}_3@g\text{-C}_3\text{N}_4$ hybrid materials at the interface between $\text{TiO}_2/\text{In}_2\text{O}_3$ and $g\text{-C}_3\text{N}_4$. These results were consistent with photocatalytic activity measurements. The $\text{TiO}_2\text{-In}_2\text{O}_3@g\text{-C}_3\text{N}_4$ photoelectrode showed much higher photocurrent intensity over binary composites, indicating that the deposition of both TiO_2 and In_2O_3 can further suppress charge recombination by improving the interfacial charge transfer under visible light irradiation. The long distance migration of photogenerated electrons and holes among TiO_2 , In_2O_3 and $g\text{-C}_3\text{N}_4$ could reduce their recombination rate. To gain further insight into the electron-transport properties of the as-prepared photocatalysts, electrochemical impedance spectroscopy (EIS) was conducted in 0.10 M KCl solution containing equimolar $[\text{Fe}(\text{CN})_6]^{3-/4-}$ at frequencies from 100 kHz to 0.1 Hz and the results presented in the form of Nyquist plots (Fig. 12B) [81]. Obviously, the arc radius decreased gradually in the order single (TiO_2 , In_2O_3 and $g\text{-C}_3\text{N}_4$) > binary ($\text{TiO}_2@g\text{-C}_3\text{N}_4$ and $\text{In}_2\text{O}_3@g\text{-C}_3\text{N}_4$) > ternary ($\text{TiO}_2\text{-In}_2\text{O}_3@g\text{-C}_3\text{N}_4$), meaning the more efficient charge separa-

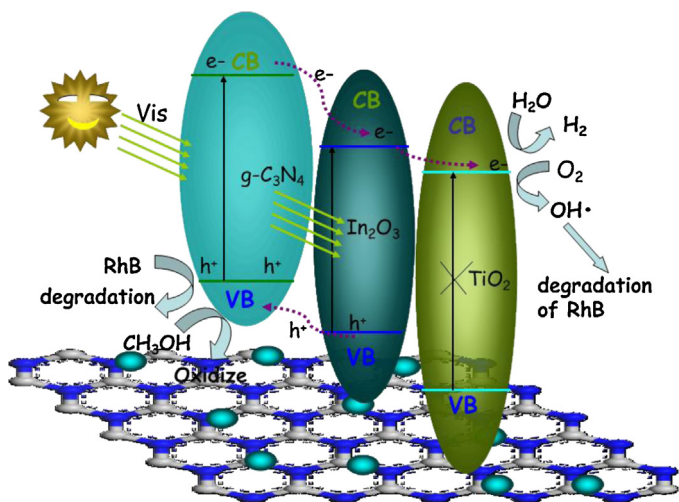


Fig. 13. Possible photocatalytic mechanism of the ternary hybrid composites.

tion occurred after coupling TiO_2 and In_2O_3 with $\text{g-C}_3\text{N}_4$, which confirmed that the synergistic impact of TiO_2 , In_2O_3 and $\text{g-C}_3\text{N}_4$ on photocatalytic activity was indispensable. Indeed, The EIS data were consistent with the results of PL and photocurrent analyses and photocatalytic activity. As a result, the enhanced photoelectrochemical properties of $\text{TiO}_2\text{-In}_2\text{O}_3\text{@g-C}_3\text{N}_4$ ternary composites could be attributed to the enhancement separation efficiency of photoinduced electrons and holes, which might attributed to the synergetic effect of TiO_2 , In_2O_3 and $\text{g-C}_3\text{N}_4$. Furthermore, the larger specific surface area could not only lead to more efficient use of the light source and enhanced light harvesting but also provide more catalytic sites [82].

3.13. Possible photocatalytic mechanism of the ternary hybrid composites

In order to explore the tentative mechanism for the enhanced photocatalytic performance of $\text{TiO}_2\text{-In}_2\text{O}_3\text{@g-C}_3\text{N}_4$, the band edge positions of the valence band (VB) and conduction band (CB) of TiO_2 , In_2O_3 and $\text{g-C}_3\text{N}_4$ were investigated. The VB edge potentials of TiO_2 , In_2O_3 and $\text{g-C}_3\text{N}_4$ at the point of zero charge can be calculated by the following empirical equation:

$$E_{\text{VB}} = X - E^e + 0.5E_g \quad (4)$$

where E_{VB} is the VB edge potential, X is the electronegativity of the semiconductor, which is the geometric mean of the electronegativity of the constituent atoms, E^e is the energy of free electrons on the hydrogen scale (~ 4.5 eV), and E_g is the band gap energy of the semiconductor. The CB edge potential (E_{CB}) can be determined by $E_{\text{CB}} = E_{\text{VB}} - E_g$. The band gaps of TiO_2 , In_2O_3 and $\text{g-C}_3\text{N}_4$ were estimated as 3.2, 2.8 and 2.7 eV, respectively, according to the previous reports [14,37,46]. Based on the band gap positions, the CB and VB edge potentials of TiO_2 (In_2O_3) were determined at -0.3 (-0.6) eV and $+2.9$ ($+2.2$) eV, respectively. The CB and VB edge potentials of $\text{g-C}_3\text{N}_4$ were at -1.2 eV and $+1.5$ eV, respectively. As depicted in Fig. 13, when the $\text{TiO}_2\text{-In}_2\text{O}_3\text{@g-C}_3\text{N}_4$ synergistic heterojunction system is irradiated with visible light, electrons are excited from the VB to the CB of In_2O_3 and $\text{g-C}_3\text{N}_4$, leaving electropositive holes at VB. The photogenerated electrons in the $\text{g-C}_3\text{N}_4$ layer structure could be easily transferred to the surface of the In_2O_3 , and then the electrons on the CB of In_2O_3 will further migrate to the CB of TiO_2 . Similarly, the holes on the VB of In_2O_3 could easily migrate to the surface of $\text{g-C}_3\text{N}_4$. Thus, this ternary system helps in the efficient electron-hole separation (evidenced using PL and photoelectrochemical measurements). The interparticle

charge transfer is promoted at the interface among TiO_2 , In_2O_3 and $\text{g-C}_3\text{N}_4$. The accumulated electrons (from In_2O_3 to $\text{g-C}_3\text{N}_4$) on the CB of TiO_2 , together with the electrons excited from the VB of TiO_2 are capable of reducing $\text{h}^+(\text{O}_2)$ into H_2 (OH^\bullet), and the OH^\bullet species are responsible for the degradation and mineralization of RhB in aqueous solution. While the corresponding accumulated and photogenerated holes on the VB of $\text{g-C}_3\text{N}_4$ can subsequently oxidize the electron donor (CH_3OH for H_2 production) and degrade RhB dye directly. At such, effectively charge separation can be achieved, resulting in longer lifetime of the photogenerated charge carriers and thus improved photocatalytic activities.

4. Conclusion

In summary, we have successfully synthesized a visible light active multifunctional ternary composite $\text{TiO}_2\text{-In}_2\text{O}_3\text{@g-C}_3\text{N}_4$ via a facile solvothermal in situ route. Compared with pure substance, the enhanced photocatalytic activity of the ternary composites towards the degradation of RhB and hydrogen generation is explained by the fast generation, separation and transportation of the photogenerated carriers as well as the higher specific surface area. The as-prepared heterostructure exhibits enough catalytic stability as evidenced by the recycling experiments. In addition, the photocurrent response of the ternary composite was stable, further indicating that the $\text{TiO}_2\text{-In}_2\text{O}_3\text{@g-C}_3\text{N}_4$ hybrid was highly suitable as a photocatalyst, performing as genuine heterogeneous visible-light-driven photocatalyst to the treatment of hazardous pollutants and solar-to-fuels conversion. This work not only highlights the potential use of $\text{TiO}_2\text{-In}_2\text{O}_3\text{@g-C}_3\text{N}_4$ ternary composites, but also provides useful information for the future design of similar multifunctional hybrids photocatalysts used in the field of environment and energy.

Acknowledgements

This work was partly supported by National Natural Science Foundation (21306067), Industry High Technology Foundation of Jiangsu Province (BE2013090), Doctoral Innovation Fund of Jiangsu (KYLX.1065), Science & Technology Foundation of Zhenjiang (SH2012011 and GY2012048) and Innovation and entrepreneurship train program (201410299054Y), China.

Appendix A. Supplementary data

Supplementary data associated with this article can be found, in the online version, at <http://dx.doi.org/10.1016/j.apcatb.2015.01.041>.

References

- [1] A. Fujishima, K. Honda, *Nature* 238 (1972) 37.
- [2] J. Yan, G. Wu, N. Guan, L. Li, *Appl. Catal. B* 280 (2014) 152–153.
- [3] M.R. Hoffmann, S.T. Martin, W. Choi, D.W. Bahnemann, *Chem. Rev.* 95 (1995) 69.
- [4] X. Chen, S. Shen, L. Guo, S.S. Mao, *Chem. Rev.* 110 (2010) 6503.
- [5] S.N. Frank, A.J. Bard, *J. Am. Chem. Soc.* 99 (1977) 303.
- [6] T.L. Thompson, J.T. Yates, *Chem. Rev.* 106 (2006) 4428.
- [7] K. Ayoub, E.D. van Hullebusch, M. Cassir, A. Bermond, *J. Hazard. Mater.* 178 (2010) 10.
- [8] S.U.M. Khan, M. Al-Shahry, W.B. Ingler, *Science* 297 (2002) 2243.
- [9] N. Semagina, L. Kiwi-Minsker, *Catal. Rev.* 51 (2009) 147.
- [10] F.S. Kim, G. Ren, S.A. Jenekhe, *Chem. Mater.* 23 (2010) 682.
- [11] A. Vaneski, A.S. Susa, J. Rodríguez-Fernández, M. Berr, F. Jäckel, J. Feldmann, A.L. Rogach, *Adv. Funct. Mater.* 21 (2011) 1547.
- [12] V. Tamilselvan, S. Kishore, K.N. Rao, P. Reji, *J. Phys. D: Appl. Phys.* 43 (2010) 385402.
- [13] R. Agarwal, C.M. Lieber, *Appl. Phys. A* 85 (2006) 209.
- [14] G. Liu, H.G. Yang, X. Wang, L. Cheng, J. Pan, G.Q. Lu, H.M. Cheng, *J. Am. Chem. Soc.* 131 (2009) 12868.

- [15] H.G. Yang, C.H. Sun, S.Z. Qiao, J. Zou, G. Liu, S.C. Smith, H.M. Cheng, G.Q. Lu, *Nature* 453 (2008) 638.
- [16] X. Han, Q. Kuang, M. Jin, Z. Xie, L. Zheng, J. Am. Chem. Soc. 131 (2009) 3152.
- [17] B. Wu, C. Guo, N. Zheng, Z. Xie, G.D. Stucky, J. Am. Chem. Soc. 130 (2008) 17563.
- [18] H.G. Yang, G. Liu, S.Z. Qiao, C.H. Sun, Y.G. Jin, S.C. Smith, J. Zou, H.M. Cheng, G.Q. Lu, J. Am. Chem. Soc. 131 (2009) 4078.
- [19] E.S. Kim, N. Nishimura, G. Magesh, J.Y. Kim, J.W. Jang, H. Jun, J. Kubota, K. Domen, J.S. Lee, J. Am. Chem. Soc. 135 (2013) 5375.
- [20] M. Long, W. Cai, J. Cai, B. Zhou, X. Chai, Y. Wu, J. Phys. Chem. B 10 (2006) 20211.
- [21] A. Kudo, Y. Miseki, Chem. Soc. Rev. 38 (2009) 253.
- [22] X.F. Gao, W.T. Sun, Z.D. Hu, G. Ai, Y.L. Zhang, S. Feng, F. Li, L.M. Peng, J. Phys. Chem. C 113 (2009) 20481.
- [23] H.J. Zhang, G.H. Chen, D.W. Bahnemann, J. Mater. Chem. 19 (2009) 5089.
- [24] A. Mukherji, B. Seger, G.Q. Lu, L. Wang, ACS Nano 5 (2011) 3483.
- [25] Z. Xiong, X.S. Zhao, J. Am. Chem. Soc. 134 (2012) 5754.
- [26] S.K. Poznyak, D. Talapin, A. Kulak, J. Phys. Chem. B 105 (2001) 4816.
- [27] X. Pan, Y. Zhao, S. Liu, C.L. Korzeniewski, S. Wang, Z. Fan, ACS Appl. Mater. Interfaces 4 (2012) 3944.
- [28] M. Huang, S. Yu, B. Li, D. Li, F. Zhang, M. Fan, L. Wang, J. Yu, C. Deng, Ceram. Int. 40 (2014) 13305.
- [29] M. Daous, V. Iliev, L. Petrov, J. Mol. Catal. A: Chem. 392 (2014) 194.
- [30] Y. Shi, H. Li, L. Wang, W. Shen, H. Chen, ACS Appl. Mater. Interfaces 4 (2012) 4800.
- [31] J. Wang, J. Huang, H. Xie, A. Qu, Int. J. Hydrogen Energy 39 (2014) 6354.
- [32] L. Baia, A. Vulpoi, T. Radu, É. Karácsónyi, A. Dombi, K. Hernádi, V. Danciu, S. Simon, K. Norén, S.E. Canton, G. Kovács, Zs. Pap Appl. Catal. B 589 (2014) 148–149.
- [33] S. Cao, C. Chen, T. Liu, B. Zeng, X. Ning, X. Chen, X. Xie, W. Chen, Catal. Commun. 46 (2014) 61.
- [34] J.B. Mu, B. Chen, M.Y. Zhang, Z.C. Guo, P. Zhang, Z.Y. Zhang, ACS Appl. Mater. Interfaces 4 (2012) 424.
- [35] L. Chen, W. Zhang, Appl. Surf. Sci. 301 (2014) 428.
- [36] T. Sreethawong, S. Ngamsinlapasathian, S. Yoshikawa, J. Colloid Interface Sci. 421 (2014) 191.
- [37] D. Shchukin, S. Poznyak, A. Kulak, P. Pichat, J. Photochem. Photobiol. A: Chem. 162 (2004) 423.
- [38] A.S. Deshpande, D.G. Shchukin, E. Ustinovich, M. Antonietti, R.A. Caruso, Adv. Funct. Mater. 15 (2005) 239.
- [39] E.V. Skorb, L.I. Antonouskaya, N.A. Belyasova, D.G. Shchukin, H. Möhwald, D.V. Sviridov, Appl. Catal. B 84 (2008) 94.
- [40] E. Wang, W. Yang, Y. Cao, J. Phys. Chem. C 113 (2009) 20912.
- [41] E. Wang, P. Zhang, Y. Chen, Z. Liu, T. He, Y. Cao, J. Mater. Chem. 22 (2012) 14443.
- [42] F. Ma, S. Zhang, X. Yang, W. Guo, Y. Guo, M. Huo, Catal. Commun. 24 (2012) 75.
- [43] M. Hinojosa-Reyes, S. Arriaga, L.A. Diaz-Torres, V. Rodríguez-González, Chem. Eng. J. 224 (2013) 106.
- [44] Z. Li, P. Zhang, J. Li, T. Shao, L. Jin, J. Photochem. Photobiol. A 271 (2013) 111.
- [45] Y. Lyu, T. Hsieh, Surf. Coat. Technol. 231 (2013) 219.
- [46] S. Zhao, S. Chen, H. Yu, X. Quan, Sep. Purif. Technol. 99 (2012) 50.
- [47] S. Yang, Y. Gong, J. Zhang, L. Zhan, L. Ma, Z. Fang, R. Vajtai, X. Wang, P.M. Ajayan, Adv. Mater. 25 (2013) 2452.
- [48] Y. Wang, X.C. Wang, M. Antonietti, Angew. Chem. Int. Ed. 51 (2012) 68.
- [49] Y. Zheng, J. Liu, J. Liang, M. Jaroniec, S.Z. Qiao, Energy Environ. Sci. 5 (2012) 6717.
- [50] J.H. Sun, J.S. Zhang, M.W. Zhang, M. Antonietti, X.Z. Fu, X.C. Wang, Nat. Commun. 3 (2012) 1139.
- [51] G. Liu, P. Niu, C. Sun, S.C. Smith, Z. Chen, G.Q. (Max) Lu, H. Cheng, J. Am. Chem. Soc. 132 (2010) 11642.
- [52] J.S. Zhang, G.G. Zhang, X.F. Chen, S. Lin, L. Möhlmann, G. Dołęga, G. Lipner, M. Antonietti, S. Blechert, X.C. Wang, Angew. Chem. Int. Ed. 51 (2012) 3183.
- [53] Y. Di, X.C. Wang, A. Thomas, M. Antonietti, ChemCatChem 2 (2010) 834.
- [54] Z.F. Jiang, X.M. Lv, D.L. Jiang, J.M. Xie, D.J. Mao, J. Mater. Chem. A 1 (2013) 14963.
- [55] X. Xu, P. Zhao, D. Wang, P. Sun, L. You, Y. Sun, X. Liang, F. Liu, H. Chen, G. Lu, Sens. Actuators B 176 (2013) 405.
- [56] S.C. Yan, Z.S. Li, Z.G. Zou, Langmuir 25 (2009) 10397.
- [57] Z.F. Jiang, J.J. Zhu, D. Liu, W. Wei, J.M. Xie, M. Chen, CrystEngComm 16 (2014) 2384.
- [58] J.H. Liu, T.K. Zhang, Z.C. Wang, G. Dawson, W. Chen, J. Mater. Chem. 21 (2011) 14398.
- [59] G.Q. Li, N. Yang, W.L. Wang, W.F. Zhang, J. Phys. Chem. C 113 (2009) 14829.
- [60] Z.F. Jiang, D. Liu, D.L. Jiang, W. Wei, K. Qian, M. Chen, J.M. Xie, Dalton Trans. 43 (2014) 13792.
- [61] G.X. Wang, X.P. Shen, J. Yao, J. Park, Carbon 47 (2009) 2049.
- [62] O. Akhavan, ACS Nano 4 (2010) 4174.
- [63] X. Bai, R. Zong, C. Li, D. Liu, Y. Liu, Y. Zhu, Appl. Catal. B 147 (2014) 82.
- [64] X. Ling, L.M. Xie, Y. Fang, H. Xu, H.L. Zhang, J. Kong, M.S. Dresselhaus, J. Zhang, Z.F. Liu, Nano Lett. 10 (2010) 553.
- [65] M. Jothibas, C. Manoharan, S. Ramalingam, S. Dhanapandian, S. Johnson Jeyakumar, M. Bououdina, J. Mol. Struct. 1049 (2013) 239.
- [66] Y. Li, H. Zhang, P. Liu, D. Wang, Y. Li, H. Zhao, Small 9 (2013) 3336.
- [67] H.J. Yan, Y. Chen, S.M. Xu, Int. J. Hydrogen Energy 37 (2012) 125.
- [68] Y.S. Xu, W.D. Zhang, ChemCatChem 5 (2013) 2343.
- [69] Y.Q. Sun, C. Li, Y.X. Xu, H. Bai, Z.Y. Yao, G.Q. Shi, Chem. Commun. 46 (2010) 4740.
- [70] D. Chandra, K. Saito, T. Yui, M. Yagi, Angew. Chem. Int. Ed. 52 (2013) 1.
- [71] J.G. Yu, L.F. Qi, M. Jaroniec, J. Phys. Chem. C 114 (2010) 13118.
- [72] Z.F. Jiang, J.M. Xie, D.L. Jiang, Z.X. Yan, J.J. Jing, D. Liu, Appl. Surf. Sci. 292 (2014) 301.
- [73] Z.F. Jiang, J.M. Xie, D.L. Jiang, J.J. Jing, H.R. Qin, CrystEngComm 14 (2012) 4601.
- [74] Z.F. Jiang, J.M. Xie, D.L. Jiang, X.J. Wei, M. Chen, CrystEngComm 15 (2013) 560.
- [75] Y.Y. Bu, Z.Y. Chen, W.B. Li, Appl. Catal. B 144 (2014) 622.
- [76] Y.J. Zhang, T. Mori, L. Niu, J.H. Ye, Energy Environ. Sci. 4 (2011) 4517.
- [77] H. Xu, J. Yan, Y. Xu, Y. Song, H. Li, J. Xia, C. Huang, H. Wan, Appl. Catal. B 129 (2013) 182.
- [78] P. Niu, L.L. Zhang, G. Liu, H.M. Cheng, Adv. Funct. Mater. 22 (2012) 4763.
- [79] C.S. Pan, J. Xu, Y.J. Wang, D. Li, Y.F. Zhu, Adv. Funct. Mater. 22 (2012) 1518.
- [80] Y.Y. Li, J.S. Wang, H.C. Yao, L.Y. Dang, Z.J. Li, Catal. Commun. 12 (2011) 660.
- [81] L. Xu, J. Xia, L. Wang, J. Qian, H. Li, K. Wang, K. Sun, M. He, Chem. Eur. J. 20 (2014) 2244.
- [82] R. Lin, L. Shen, Z. Ren, W. Wu, Y. Tan, H. Fu, J. Zhang, L. Wu, Chem. Commun. 50 (2014) 8533.